

Spectral stochastic estimation of high-Reynolds-number wall-bounded turbulence for a refined inner-outer interaction model

Woutijn J. Baars,^{*} Nicholas Hutchins, and Ivan Marusic

Department of Mechanical Engineering, University of Melbourne, Victoria 3010, Australia

(Received 31 May 2016; published 23 September 2016)

For wall-bounded flows, the model of Marusic *et al.* [[Science](#) **329**, 193 (2010)] allows one to predict the statistics of the streamwise fluctuating velocity in the inner region, from a measured input signal in the logarithmic region. Normally, a user-defined large-scale portion of the input forms the large-scale content in the prediction by scaling its amplitude, as well as temporally shifting the signal to account for the physical inclination of these scales. Incoherent smaller scales are then fused to the prediction via universally expressed fluctuations that are subject to an amplitude modulation. Here we present a refined version of the model using spectral linear stochastic estimation, which eliminates a user-defined scale separation of the input. Now, an empirically derived transfer kernel comprises an implicit filtering via a scale-dependent gain and phase; this kernel captures the coherent portion in the prediction. An additional refinement of the model embodies a relative shift between the stochastically estimated scales in the prediction and the modulation envelope of the universal small scales. Predictions over a three-decade span of Reynolds numbers, $Re_\tau \sim O(10^3)$ to $O(10^6)$, highlight promising applications of the refined model to high-Reynolds-number flows, in which coherent scales become the primary contributor to the fluctuating energy.

DOI: [10.1103/PhysRevFluids.1.054406](https://doi.org/10.1103/PhysRevFluids.1.054406)

I. INTRODUCTION

Large-scale coherence in high-Reynolds-number wall turbulence has been evidenced by flow structures that comprise a hierarchical ordering of scales in the wall-normal direction, significant lifetimes in the streamwise direction, and an arrangement in both the spanwise and streamwise directions [1–8]. This large-scale organization of the flow is pronounced in the logarithmic region of turbulent boundary layers (TBLs), where turbulent kinetic energy is primarily comprised of large-scale energy [8]. Although small-scale turbulence is naturally less coherent, a strong linkage between large-scale motions and smaller-scale velocity fluctuations has been observed [9–11]. Hutchins and Marusic [8,12] emphasized how the amplitude of the large-scale fluctuations is related to the magnitude of the small-scale intensity. This direct linkage between the large and small scales is considered an amplitude modulation [13]. Recent studies have concentrated on the modulation mechanism in TBLs in an attempt to quantify this scale interaction [13–16]. Baars *et al.* [17] accentuated that modulation, compliant with the framework of Chernyshenko *et al.* [18] and Zhang and Chernyshenko [19], is a mechanism confined to a layer below the onset of the log region, while a preferential arrangement, or alignment of the small scales relative to the large scales, prevails in the log region and beyond. In 2010 Marusic *et al.* [20] merged the facets of large-scale coherence and the linkage between the small and large scales in TBLs to form a predictive model for turbulence (referred to hereafter as the MMH model). Statistics of the fluctuating streamwise velocity in the inner region of wall-bounded flows can be predicted from an acquired large-scale velocity signal in the outer region.

Prior to 2010, models had long been proposed to predict statistics of wall-bounded flows. These models typically comprised propositions for the scaling of turbulence intensity profiles; see the review by Smits *et al.* [21] and a series of individual contributions proposing inner scaling, outer scaling, and combinations of those two (see Refs. [22–24]). Evidently, formulations for higher-order

^{*}wbaars@unimelb.edu.au

turbulence statistics and spectra were absent in many of the scaling-type arguments. Modeling efforts of wall turbulence have been stimulated further by the improbable scenario of fully resolving the dynamics of all turbulent scales at high Reynolds numbers, via both numerical and experimental efforts. An increasing friction Reynolds number, defined as $\text{Re}_\tau \equiv \delta U_\tau / \nu$, implies a larger range of energetic turbulent scales, conceptually bounded by the outer and inner length scales. The outer scale, δ , is the boundary layer thickness, and the inner scale is taken as the fluid kinematic viscosity, ν , divided by $U_\tau \equiv \sqrt{\tau_w / \rho}$, where τ_w is the mean wall-shear stress and ρ is the fluid density. While direct numerical simulations are limited by computational requirements at high Re_τ [25–29], experimental efforts to fully resolve the wall-turbulence statistics are affected by instrumentation limits. Most notably, hot-wire anemometry is affected by sensor spatial and temporal resolution limits [30], whereas particle image velocimetry methods are limited by their dynamic range. In addition, wall-proximity errors and physical dimensions of the instrument itself dictate the minimum wall-normal distance at which measurements are feasible. In light of the experimental and numerical challenges, empirical development of models for wall-turbulence statistics is crucial [20,31,32]. We here present a refined predictive capability of the MMH model by assessing the coherent nature of the wall turbulence. Before providing an outline of our paper we review the MMH model.

A. Review of the MMH model

For wall turbulence, the MMH model has the ability to predict the statistics of the fluctuating streamwise velocity in the inner region from an outer region input; all technical intricacies are described by Mathis *et al.* [33,34]. Nominally, the inner region spans $0 < z^+ < 0.15\text{Re}_\tau$, whereas the outer region spans the log region and above. The MMH model is expressed by

$$u_p^+(z^+) = \underbrace{u^*\{1 + \beta u_{OL}^+(z_O^+, \theta_L)\}}_{\text{modulation}} + \underbrace{\alpha u_{OL}^+(z_O^+, \theta_L)}_{\text{superposition}}. \quad (1)$$

Here u_p^+ is the predicted streamwise fluctuating velocity signal u^+ at z^+ . The $+$ superscript denotes a normalization with inner scales, which for the wall-normal coordinate entails $z^+ \equiv zU_\tau/\nu$ and for the velocity fluctuation, $u^+ \equiv u/U_\tau$. A large-scale signal, u_{OL}^+ , acquired at an outer-region position, z_O^+ , is the only user input required. Subscript O refers to the outer-region position, whereas subscript L refers to a long-wavelength pass filter. Commonly, the raw input signal, u_O^+ , is spectrally filtered to retain large scales at streamwise wavelengths larger than $\lambda_{x_F}^+ \equiv \lambda_{x_F} U_\tau/\nu = 7000$. Here the local mean velocity, $U_m^+(z_O^+)$, is used in determining the separation frequency, $f^+ \equiv U_m^+/\lambda_x^+$. An argument for the value of $\lambda_{x_F}^+$ is that the small scales are incoherent over the prediction distance, $\Delta z^+ = |z_O^+ - z^+|$. Hence, these incoherent scales have to be modeled and expressed in universal form. The inner-scaled universal velocity signal u^* , and coefficients α , β , and θ_L , are deduced from a calibration experiment involving two-point measurements of the streamwise velocity fluctuations [33]. Note that all velocity fluctuations in Eq. (1), being u_p^+ , u^* and u_{OL}^+ , are time series with a synchronized inner-scaled time coordinate, $t^+ \equiv tU_\tau^2/\nu$, and that u^* , α , β , and θ_L are all functions of z^+ . We may rewrite the MMH expression as

$$u_p^+(z^+) = u^*\{1 + \Gamma u_S^+\} + u_S^+, \quad (2)$$

where coefficient $\Gamma = \beta/\alpha$ and $u_S^+ = \alpha u_{OL}^+(z_O^+, \theta_L)$; note that the arguments are omitted for simplicity. Equation (2) is visualized by the flow diagram in Fig. 1.

As is apparent from Eq. (1), two additive components form the MMH model prediction. Term $u_S^+ = \alpha u_{OL}^+(z_O^+, \theta_L)$ models a superposition effect. That is, the large-scale signature perceived at prediction location z^+ is directly induced by the large-scale turbulence acquired at z_O^+ with a gain factor equal to α . Parameter θ_L that appears as an argument of u_{OL}^+ represents the mean inclination angle of the large-scale structures throughout the boundary layer [35]. Since the outer-region signal, u_{OL}^+ , is equated to a position closer to the wall, the signal is shifted according to this mean inclination. The second component of the MMH model constitutes the $u^*\{1 + \Gamma u_S^+\}$ term in Eq. (2). It is

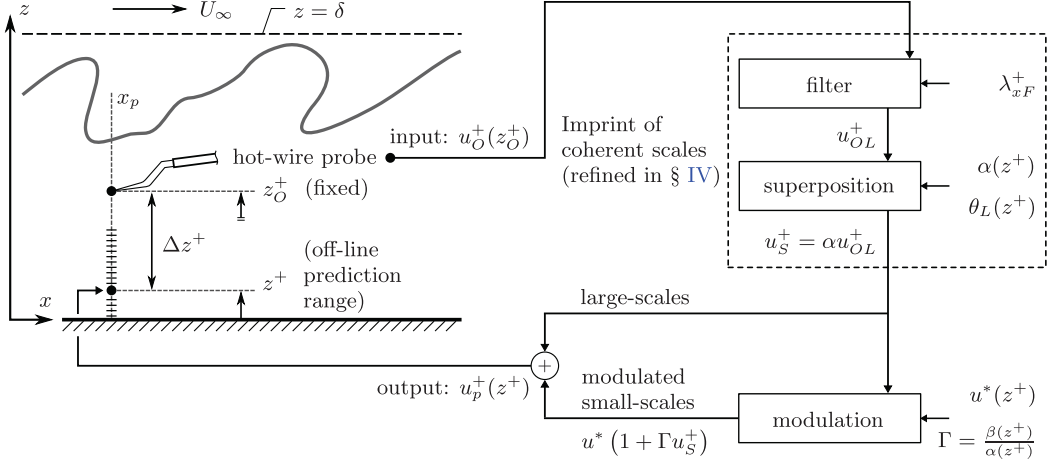


FIG. 1. Flow diagram of the MMH model [20] for predicting a statistically realistic velocity signal in the inner region, $u_p^+(z^+)$, from an input signal acquired in the outer region, $u_o^+(z_0^+)$.

straightforward that this part of the model encompasses an amplitude modulation of the universal signal, u^* , where the large-scale induced signature, u_S^+ , acts as the modulation envelope, with a strength given by coefficient Γ (Fig. 1). Consequently a critical part of the model is to predict the imprint of the large scales, u_S^+ , from the input at z_0^+ , as this is used in both the modulation and superposition components of the MMH model.

B. Outline of the paper

A refined procedure for obtaining u_S^+ is introduced in the current work. How the velocity fluctuations at z_0^+ are coupled with the fluctuations at other positions, z^+ , is analyzed via linear system theory (Sec. III A) applied to two-point time-resolved data (Sec. II). Formulating the problem in terms of an input-output system is beneficial when the coupling is to be expressed in terms of a transfer kernel. To achieve this, we will introduce a first order (linear) stochastic estimation approach in spectral space (Sec. III B), generally known as spectral linear stochastic estimation (LSE) [36–38]. We present the adjusted model in Sec. IV A and describe in Sec. IV B how the new model calibration parameters are extracted. Predictions are then performed in Sec. V for ZPG TBL flows covering a three-decade span of Reynolds numbers, $\text{Re}_\tau \sim O(10^3)$ to $O(10^6)$.

II. TWO-POINT TIME-RESOLVED DATA

To glean an understanding of the coupling between the velocity fluctuations at z_0^+ and other positions, we rely on synchronized two-point measurements. These data are the foundation for the MMH model, and its refined version, and are in fact a prerequisite for model calibration (see Ref. [33] and Sec. IV B). Data were acquired in Melbourne’s boundary layer facility [39,40]. Its test section inlet at $x = 0$ m (where x is the streamwise coordinate) has a cross-sectional area of 1.89 (width) \times 0.92 (height) m^2 . On the wind tunnel floor and side walls, the boundary layer is tripped using a 154 mm streamwise section of P40 grit sandpaper, after which the layer develops naturally down the 27 m long test section. An adjustable ceiling with bleeding slots was positioned for a nominal ZPG in the x direction; pressure coefficient, C_p , was constant to within $\pm 0.87\%$ [41]. Free-stream turbulence intensities were less than 0.05% of the free stream at $x = 0$ m and remained in the range 0.15–0.20 % at $x \approx 18$ m. Two data sets are employed in the current study and comprise two-point hot-wire arrangements as schematically shown in Fig. 2(a); experimental parameters of the data are listed in Table I.

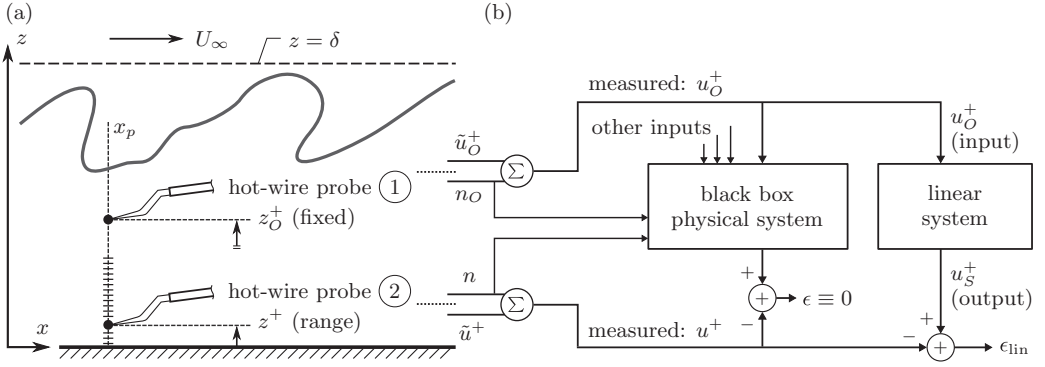


FIG. 2. (a) Experimental arrangement of the two-probe hot-wire measurements in Melbourne's boundary layer facility; see Table I for a listing of the relevant parameters. (b) Considering the synchronously acquired two-probe hot-wire signals as a single-input and single-output (SI/SO) system. Under ideal conditions, a black box physical system can predict the measured output, u , with zero error, while a linear system simplification may result in an error $\epsilon_{lin} = |u_S^+ - u^+|$.

The first data set is taken from Mathis *et al.* [33] and was acquired at $Re_\tau \equiv \delta U_\tau / \nu = 7350$. Here δ is the boundary layer thickness computed from a modified Coles law of the wake fit [42], and U_τ was found from a Clauser chart fit with log-law constants $\kappa = 0.41$ and $A = 5.0$. Each of the two Wollaston wires (silver-coated platinum) were etched to expose a sensing element with a constant viscous scaled length of $l^+ \equiv lU_\tau / \nu \approx 22$. Wires with a diameter of $d = 5 \mu\text{m}$ obeyed the $l/d \geq 200$ criterion [43] and were operated in constant temperature mode using an in-house built anemometer (MUCTA) [30]. The bottom and top hot-wire probes were positioned at the same streamwise position ($x_p = 21$ m) and at the spanwise center of the tunnel. Each probe could be moved independently in

TABLE I. Experimental parameters of two-point hot-wire data acquired in Melbourne's boundary layer facility.

		Data set: $Re_\tau \approx 7350$ [33]		
Boundary layer		Hot wire	Top (1)	Bottom (2)
x_p	21 m	l^+	22	22
U_∞	10.02 m/s	l/d	200	200
δ	0.328 m	ΔT^+	0.32	0.32
U_τ	0.338 m/s	TU_∞/δ	18 300	18 300
ν/U_τ	44.6 μm	z_O^+	441 ^c	–
$3.9Re_\tau^{1/2}$	334	z^+	–	[6.28, 359] ^a
		Data set: $Re_\tau \approx 13\,300$		
Boundary layer		Hot wire	Top (1)	Bottom (2)
x_p	21 m	l^+	21	21
U_∞	20.35 m/s	l/d	200	200
δ	0.321 m	ΔT^+	0.61	0.61
U_τ	0.651 m/s	TU_∞/δ	22 900	22 900
ν/U_τ	24.1 μm	z_O^+	469 ^c	–
$3.9Re_\tau^{1/2}$	450	z^+	–	[10.5, 379] ^b

^aRange in the wall-normal direction, z , spanned by 25 logarithmically spaced measurement points.

^bWall-normal range spanned by 24 logarithmically spaced points.

^cAlthough we consider locations $z^+ \leq z_O^+$, z profiles were acquired up to the free stream in order to compute δ .

the wall-normal direction using two separate traverse systems: a tunnel-specific traverse for the top probe, labeled 1, and a wall-implemented traverse for the bottom probe, labeled 2 [see Fig. 2(a)]. During data acquisition, probe 1 was kept at $z_O^+ = 441$; this position bears relevance to the location of the model's input signal (see Ref. [33] and Sec. IV A). Probe 2 was traversed in the inner region with 25 logarithmically spaced points in the range $6.28 \leq z^+ \leq 359$. Regarding data acquisition, both wires were sampled simultaneously at a rate of $\Delta T^+ \equiv U_\tau^2/\nu/f_s \approx 0.32$, where f_s is the sampling frequency, and guaranteed an absence of temporal attenuation [30]. To prevent aliasing, the signals were passed through fourth-order Butterworth filters, with a spectral cutoff set at $f_s/2$, prior to A/D conversion using a 16-bit Data Translation DT9836 module. Relatively long signals were acquired with a length of $TU_\infty/\delta \approx 18\,300$; this enables us to obtain converged spectral statistics at the largest energetic wavelengths. Before and after the measurement, both hot-wire probes were calibrated at a range of free-stream velocities against a Pitot-static tube situated at $z = 0.525$ m.

Two-point measurements were repeated at $\text{Re}_\tau \approx 13\,300$. Acquisition details are identical to the data described above [33], with a few exemptions. A recent added feature to Melbourne's boundary layer facility is a floating element drag balance that is capable of measuring the wall drag of both smooth and rough walls [40]. Hence, the friction velocity was inferred from a direct survey of the wall-shear stress, while a modified Coles law of the wake fit was still used to determine δ . Since the previous data ($\text{Re}_\tau \approx 7350$) were acquired at the same position, its associated friction velocity can be derived from friction data as a function of unit Reynolds number, U_∞/ν [40], and results in $U_\tau = 0.340$ m/s. This value of U_τ agrees to within $\sim 0.6\%$ with the value obtained via the modified Coles law of the wake fit (Table I). Regarding the $\text{Re}_\tau \approx 13\,300$ data, two $d = 2.5$ μm platinum wires with an $l/d = 200$ ratio were used so that their viscous scaled lengths matched those of the $\text{Re}_\tau \approx 7350$ data. A calibration method with corrections for hot-wire voltage drift was implemented as follows. The top probe was moved to the free stream after every five measurement points, while the bottom probe was moved simultaneously to z_O^+ . Mean voltages of both probes were then logged for 60 sec to correct for drift [44], although this correction does not alter any of the results. Finally, we ensured that the intrusive hot wires had a minimal impact on one another by employing probe holders with a length greater than one TBL thickness. A minimum separation distance, $\Delta z_{\min}^+ = z_O^+ - z_{\max}^+ = 90$ (physically $\Delta z_{\min} = 2.2$ mm), was dictated by the prong size of the Dantec 55P15 probes.

III. IMPRINT OF COHERENT SCALES

A. Single-input and single-output system analysis

To explore the coupling of wall-turbulence dynamics between the input (z_O^+) and output (z^+) locations encountered during a model prediction, we examine the synchronized two-point data as a single-input and single-output (SI/SO) system, as shown in Fig. 2(b). Stationary streamwise velocity fluctuations, u_O^+ and u^+ , with zero mean values, correspond to probe locations 1 and 2, respectively. Noise components, n_O and n , may be present, meaning that the true velocity fluctuations, \tilde{u}_O^+ and \tilde{u}^+ may be affected. Nonetheless, our current measurement technique of hot-wire anemometry is a well-validated technique at the Reynolds numbers of our study [30], yielding negligible noise. Moreover, additive noise in system analysis may not affect the quantification of input-to-output coupling in terms of a transfer function, depending on the correlation characteristics of the noise components relative to one another and the true signals [45]. Throughout the remainder of this section we illustrate the relevant features of our SI/SO analysis for one specific output location in our $\text{Re}_\tau \approx 13\,300$ data set. We chose the position closest to the wall as the output location ($z^+ \approx 10.5$), while the input location ($z_O^+ \approx 469$) resides in the log region at $z^+ = 3.9\text{Re}_\tau^{1/2} \approx 450$ [33]. Time series of both input and output velocity fluctuations are shown in Fig. 3(a) with gray lines. Spectral representations of u_O^+ and u^+ are depicted in Fig. 3(b) in terms of the premultiplied energy spectra. For reference, large-scale components of u_O^+ and u^+ are shown with dash-dot lines in Fig. 3(a) following the filter operation that is a prerequisite of the MMH model (Sec. IA). It has to be noted that we transform frequency to wavelength, $f^+ \rightarrow \lambda_x^+$, for spectral plots throughout the paper to

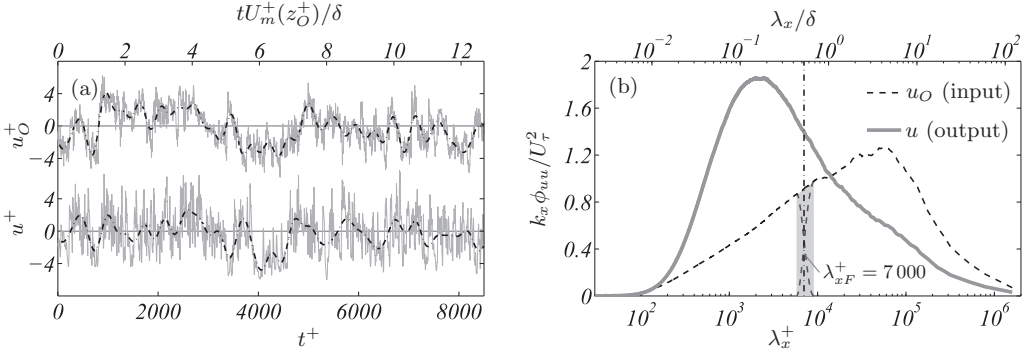


FIG. 3. (a) Time series of an input, $u_O^+(z_O^+)$, and output, $u^+(z^+ \approx 10.5)$, for SI/SO system analysis ($\text{Re}_\tau \approx 13300$ data). (b) Premultiplied energy spectra of the input and output. A spectral scale separation is shown for the input spectrum around λ_{xF}^+ ; time series of the large-scale components of both u_O^+ and u^+ are shown in subfigure (a) with the *dash-dot lines*. Inner-scaled wavelength is computed using the mean velocity at position z_O^+ , following $\lambda_x^+ \equiv U_m^+(z_O^+)/f^+$.

interpret scale as a physical size. This change of visual reference frame ($\lambda_x^+ \propto 1/f^+$) does not have any consequences for model predictions.

A routine objective in system analysis is to predict the system’s output from the input. A black box physical system in Fig. 2(b) represents an *ideal* plant that predicts an output that is equal to the measured response, u^+ , hence the defined zero-valued error, $\epsilon \equiv 0$. Such a system incorporates the coherent physics relating the true SI/SO fluctuations and accounts for any incoherent features that cannot be predicted via linear or nonlinear schemes, e.g., by way of universal models. For broadband turbulence it has proven elusive to capture a mathematical or empirical description of such a system, but system analysis techniques can partially fill this void. In the current work we confine ourselves to a linear system technique. The output of the linear time invariant system [Fig. 2(b)] is denoted as estimate u_S^+ and differs from the measured output by error ϵ_{lin} . Here subscript “lin” refers to the linear system being employed and subscript S refers to the superposition component of the IOIM (in Sec. IV A, the linear estimate forms the superposition component). A Volterra functional series may be used to describe the linear system and yields [45,46]

$$u_S^+(t^+) = \int h_1(\tau^+) u_O^+(t^+ - \tau^+) d\tau^+. \quad (3)$$

Output $u_S^+(t^+)$ is constructed from a convolution of the input signal with a first-order transfer kernel, $h_1(\tau^+)$. Since the output is proportional to u_O^+ , with a gain factor given by the transfer kernel as a function of temporal offset τ between the input and output, the convolution accounts for just the linear mechanism of energy transfer. When higher-order terms are preserved in Eq. (3), the analysis enables nonlinear energy transfer. Inevitably, higher-order schemes increase the system’s complexity while they may not improve the estimate. A number of studies in wall-bounded turbulence have concentrated on higher-order estimation schemes. Most notably, Naguib *et al.* [47] formulated a time-domain quadratic scheme that comprised estimates of the velocity field in a TBL, given surface pressures as an input; their stochastic estimates became more accurate upon inclusion of the quadratic terms. Likewise, pressure-velocity estimates have been performed for cavity flow configurations [48–50] and backward facing steps [51]. For detailed intricacies of higher-order techniques, the reader is referred to the credited work above and the discussion by Baars and Tinney [52]. Naguib *et al.* [47] revealed that the significant improvement of the quadratic estimate, relative to the linear one, is linked to the source of the wall-pressure field comprising a quadratic mechanism in the velocity field. On the other hand, when using velocity as input, Guezennec [53] showed a negligible improvement in the estimate of TBL velocity fields when quadratic terms were

preserved. Similarly, Adrian *et al.* [54] mentioned the remarkable agreement between LSE and conditional averaged fields in channel flow. Given our current interest of estimating the near-wall imprint of velocity scales from *velocity* recordings in the log region of TBLs, we proceed with the linear system simplification in Sec. III B. Moreover, the superposition component of the MMH model is formed by a linear technique (Sec. III B 2) and has proven to be sufficient for accurate predictions.

B. Refined imprint of coherent scales

Here we are concerned with estimating the velocity signal in the near-wall region from a velocity measurement in the outer region. First, a brief review of stochastic estimation in turbulence is provided. Hereafter, in Sec. III B 1, we apply an LSE scheme to the input and output signals shown in Fig. 3 to illustrate the new superposition procedure of the model; a number of beneficial aspects are discussed in Sec. III B 3.

Over the past few decades, stochastic estimation techniques have been applied extensively to turbulent flows to study their coherent structure; applications include the work by Adrian [36], Adrian and Moin [55], Cole and Glauser [56], Bonnet *et al.* [57], and others. In its simplest form, LSE is applied with a single gain factor at one temporal offset, which was dubbed single-time LSE [in this case the transfer function in Eq. (3), h_1 , becomes a delta function]. When multiple temporal offsets are considered, each associated with their respective gain factor, the technique is known as multitime LSE. Ewing and Citriniti [37] carried out a comparison between velocity-velocity single-time and multitime LSE in an annular shear layer. As anticipated, the multitime LSE scheme reduced the estimate error. Spectral LSE (SLSE) as described by Tinney *et al.* [38] performs the multitime estimate efficiently in the frequency domain and is associated with reduced complexity, since the convolution integral in Eq. (3) transforms to a multiplication of the spectral input and scale-dependent transfer kernel.

1. Spectral linear stochastic estimation (SLSE)

In order to inspect whether the system's input $u_o^+(z_o^+)$ and output $u^+(z^+)$ are coupled we consider the linear coherence spectrum (LCS). In essence, the LCS reflects the maximum correlation coefficient for each Fourier scale and is insightful for the spectral framework of SLSE. The LCS for the SI/SO is given by [45]

$$\gamma^2(f^+) = \frac{|\langle U_o(f^+) \overline{U(f^+)} \rangle|^2}{\langle |U_o(f^+)|^2 \rangle \langle |U(f^+)|^2 \rangle}, \quad (4)$$

where $U(f^+) = \mathcal{F}[u^+(t^+)]$ is the Fourier transform of u^+ , $\langle \rangle$ denotes ensemble averaging, the overbar indicates the complex conjugate and $||$ designates the modulus. And so, the LCS is the ratio of the cross-spectrum magnitude, squared, relative to the product of the power spectral densities of u_o^+ and u^+ . Throughout our work, temporal realizations of $N = 2^{17}$ samples are used with a 50% overlap, resulting in approximately 210 and 230 ensembles for the $\text{Re}_\tau = 7350$ and $\text{Re}_\tau \approx 13\,300$ data sets, which ensures converged spectral statistics at the largest energetic wavelengths. In Fig. 4 we show a raw coherence spectrum (γ_{raw}^2) alongside a filtered version (γ_{filt}^2). For the latter, a bandwidth moving filter (BMF) of 25% is exercised, meaning that γ_{filt}^2 at wavelength $\lambda_{x_i}^+$ is equal to the average of the unfiltered spectrum over span $\lambda_{x_i}^+ \pm 25\%$.

Considering that γ^2 is bounded by 0 (an absence of coherence) and 1 (perfect coherence), an apparent trend of increasing coherence with increasing wavelength is observed in Fig. 4. This trend is anticipated for any spatially separated two-point measurement in a turbulent flow due to the smaller turbulent eddies comprising smaller integral time scales, hence resulting in lower correlations over a fixed separation distance. The largest energetic input and output scales possess a strong linear coherence of ~ 0.8 . An upsurge of coherence for $\lambda_x^+ < 50$ is caused by coherent noise in the measurement system and resides close to the experimental Nyquist frequency (energy levels are small; see Fig. 3). For reasons discussed later, we identified a spectral scale (denoted as λ_{xT}^+), using

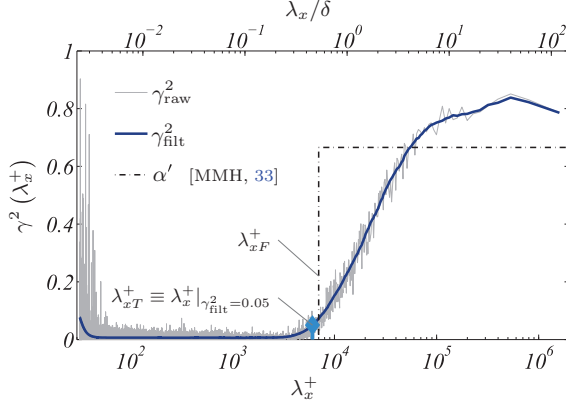


FIG. 4. Linear coherence spectrum (LCS) for the input and output signals shown in Fig. 3. A 25% bandwidth moving filter (BMF) is used to construct the filtered LCS (γ_{filt}^2) from the raw LCS (γ_{raw}^2). For a threshold value of $\gamma_{\text{filt}}^2 = 0.05$ we have marked the affiliated spectral scale (λ_{xT}^+). In consideration of the MMH model (Sec. III B 2), the magnitude of correlation coefficient α' is shown for $\lambda_x^+ > \lambda_{xF}^+ = 7000$. Inner-scaled wavelength is computed using the mean velocity at position z_0^+ , following $\lambda_x^+ \equiv U_m^+(z_0^+)/f^+$.

a coherence threshold of $\gamma_{\text{filt}}^2 = 0.05$, for which the coherence becomes negligible; we employ λ_{xT}^+ in the SLSE framework outlined next.

The significant linear coupling for the SI/SO system warrants the application of SLSE. When Fourier transforming Eq. (3) to the spectral domain we obtain the following SLSE expression [38,45]:

$$U_S(f^+) = H_L(f^+)U_O(f^+). \quad (5)$$

Here H_L is the complex-valued linear transfer kernel. During estimation, the conditional spectral output, U_S , is estimated from the unconditional input, U_O . Following linear system analysis [45,58], the transfer kernel is solved using synchronized input-output data. After multiplying Eq. (5) by the complex conjugate of the spectral input, $\overline{U_O}$, and taking the output as the unconditional spectral output, U , ensemble averaging results in

$$H_L(f^+) = \frac{\langle U(f^+)\overline{U_O(f^+)} \rangle}{\langle U_O(f^+)\overline{U_O(f^+)} \rangle} = |H_L(f^+)|e^{j\phi(f^+)}. \quad (6)$$

Equation (6) is an explicit expression for obtaining H_L and is equal to the input-output cross-spectrum, divided by the input spectrum. The complex-valued kernel includes the system's gain, being the modulus, via

$$|H_L(f^+)| = \frac{|\langle U(f^+)\overline{U_O(f^+)} \rangle|}{\langle |U_O(f^+)|^2 \rangle}, \quad (7)$$

and the phase of the kernel is equal to the phase of the cross-spectrum:

$$\phi(f^+) = \text{atan} \left\{ \frac{\Im[\langle U(f^+)\overline{U_O(f^+)} \rangle]}{\Re[\langle U(f^+)\overline{U_O(f^+)} \rangle]} \right\}. \quad (8)$$

Intuitively, the system's gain is related to the LCS, scaled by the ratio of input-to-output energies, following [45]

$$|H_L(f^+)| = \sqrt{\gamma^2(f^+) \frac{\langle |U(f^+)|^2 \rangle}{\langle |U_O(f^+)|^2 \rangle}}. \quad (9)$$

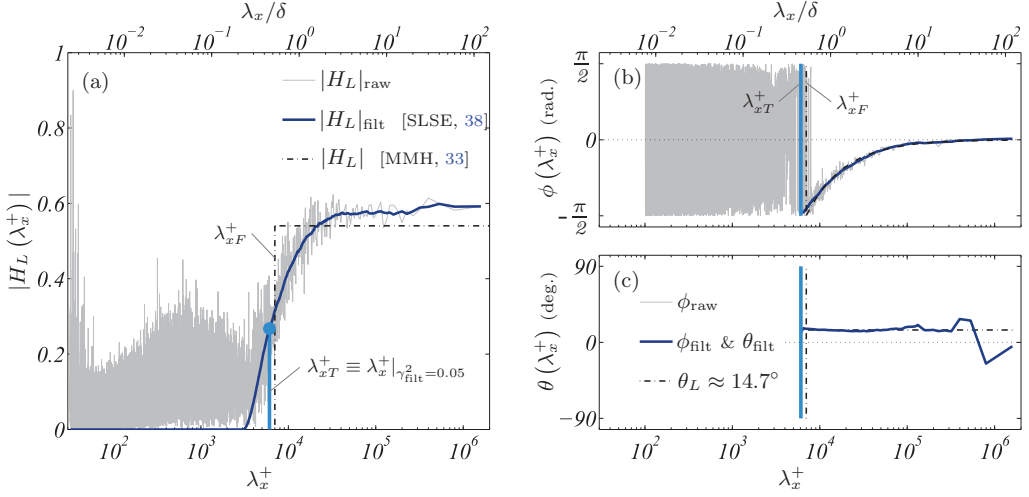


FIG. 5. (a) Linear gain for the input and output signals shown in Fig. 3. A filtered gain factor, $|H_L|_{\text{filt}}$, is composed of the filtered (25% BMF) raw gain, $|H_L|_{\text{raw}}$, that is enforced to gradually roll-off to a zero gain for $\lambda_x^+ < \lambda_{xT}^+$ (described in the text). In consideration of the MMH model (Sec. III B 2), the gain employed by Marusic *et al.* [20] (MMH) is shown for $\lambda_x^+ > \lambda_{xF}^+$. (b) System's phase in radians (legend shown in subfigure c). (c) Phase expressed as a physical inclination angle θ . Filtered phases, with a 25% BMF, are shown for $\lambda_x^+ > \lambda_{xT}^+$; a constant inclination angle, θ_L , is indicated for comparison [20]. Inner-scaled wavelength is computed using the mean velocity at position z_0^+ , following $\lambda_x^+ \equiv U_m^+(z_0^+)/f^+$.

Plots of the raw gain and phase are shown in Figs. 5(a) and 5(b), respectively. At the largest wavelengths, the gain factor plateaus near ~ 0.6 , while a roll-off occurs for $\lambda_x^+ \lesssim \lambda_{xT}^+$ (associated with a vanishing coherence; see Fig. 4). Despite the fact that the raw gain may be used for SLSE, the inconsistent gain factor yields spurious estimates at wavelengths $\lambda_x^+ \lesssim \lambda_{xT}^+$, since incoherent fluctuations may propagate into the conditional output with a gain factor of 0 to ~ 0.2 . Specifically, there is no linear mechanism of energy coupling at these scales when there is no coherence, which manifests as an inability to estimate any physically representative fluctuations of these scales. Tinney *et al.* [38] proposed to alter the gain to prevent estimation of incoherent events, by setting the gain equal to zero when the coherence does not exceed a threshold. We adopt this concept by enforcing a decay to zero of the 25% bandwidth moving filtered gain, in the vicinity of λ_{xT}^+ , as is illustrated by $|H_L|_{\text{filt}}$ in Fig. 5(a). Due to the natural decay of the LCS, results are insensitive to the choice of a sensible threshold. In summary, the linear gain highlights that all coherent large scales, recorded in the outer region (z_0^+), are superposed at the near-wall position (z^+) with a weighting of ~ 0.6 .

While the transfer gain embeds the *scaling* of each Fourier component in the estimate, the *shift* of each Fourier mode is embedded in the phase, $\phi(f^+)$. This phase is shown in Fig. 5(b) as radians of the period of each Fourier component (the inner-normalized time period is equal to $1/f^+$). It is instructive to compute a temporal shift τ , from the radial phase, by premultiplying the phase by its period: $\tau^+ = \phi(f^+)/(2\pi f^+)$. In order to then obtain a physical inclination angle, we follow the literature by using $\theta \equiv \tan^{-1}[\Delta z/(\tau U_c)]$ [35,59]. Here Δz is the spatial separation between u_0^+ and u^+ , and U_c is a convective speed, taken as the mean velocity at z_0^+ . Angle θ , computed from the filtered phase, ϕ_{filt} , is shown in Fig. 5(c). A positive θ corresponds to a spatially forward-leaning structure. A scalar inclination angle obtained from a two-point correlation of the large-scale velocity signals (large-wavelength-pass filtered at $\lambda_{xF}^+ = 7000$) is equal to $\theta_L \approx 14.7^\circ$ [shown in Fig. 5(c)]. It is evident that the coherent scales obey a virtually constant angle by inspecting profile θ_{filt} , meaning that those nondispersive scales are superposed at z^+ with an almost equal shift.

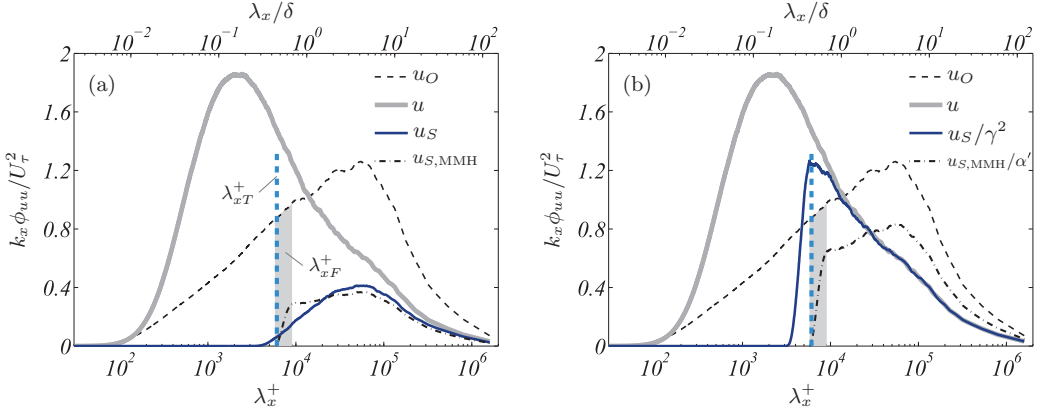


FIG. 6. (a) Energy spectra of the SLSE estimate, u_S , and the input and output. In consideration of the MMH model (Sec. III B 2), the spectrum of the superposition estimate is shown: $u_{S,MMH}$. (b) Similar to subfigure (a), but the spectra of the estimates are scaled with their respective coherence factors: $1/\gamma^2(f^+)$ and $1/\alpha'$ for the u_S and $u_{S,MMH}$ spectra, respectively. Inner-scaled wavelength is computed using the mean velocity at position z_0^+ , following $\lambda_x^+ \equiv U_m^+(z_0^+)/f^+$.

For SLSE we use a combination of the filtered gain factor and the original phase to form a new kernel:

$$\tilde{H}_L(f^+) = |H_L(f^+)|_{\text{filt}} e^{j\phi(f^+)}. \quad (10)$$

Although an inconsistent phase exists at the smaller wavelengths, it will not impact the estimation due to the zero-valued gain factor at these incoherent wavelengths. Hence, the original, raw phase is considered since filtering the phase is unnecessary and may pose challenges when ϕ crosses the $\pi/2$ boundaries. After the kernel is computed from synchronized two-point data, a conditional estimate of the spectral output, U_S , is found from the unconditional input via

$$U_S(f^+) = \tilde{H}_L(f^+)U_O(f^+) = \tilde{H}_L \mathcal{F}[u_O^+(t^+)]. \quad (11)$$

Finally, the time-domain conditional estimate is obtained by the inverse Fourier transform:

$$u_S^+(t^+) = \mathcal{F}^{-1}[U_S(f^+)]. \quad (12)$$

A premultiplied energy spectrum of the conditional estimate (signal u_S) is shown in Fig. 6(a), alongside the input and output spectra. Equation (11) implies that the estimated spectrum is equal to the input spectrum, multiplied by $|\tilde{H}_L(f^+)|^2$. In addition, it is shown in Fig. 6(b) that when the estimated spectrum is scaled by a factor that would account for the imperfect linear coherence, being the inverse of the LCS following $1/\gamma^2(f^+)$, the estimated spectrum follows the measured spectrum. In other words, the linearly estimated spectrum constitutes less energy due to the lack of perfect coherence [the visual implication of Eq. (9)]. As discussed in Sec. III A, inclusion of nonlinear terms in the stochastic estimate are not expected to improve the velocity estimate. In consideration of the model's objective, the total spectral energy of the output signal may be obtained by incorporating the incoherent small scales in a universally expressed signal, u^* . Finally, it is worth noting that our input and output locations exhibit a relatively large spatial separation ($\Delta z^+ \approx 459$), which implies a relatively low-amplitude coherence. Subsequently, only a relatively low fraction of the output energy (~ 0.8 at the larger wavelengths, equal to the amplitude of the LCS in Fig. 4) is accounted for during the SLSE for this particular combination of input and output locations.

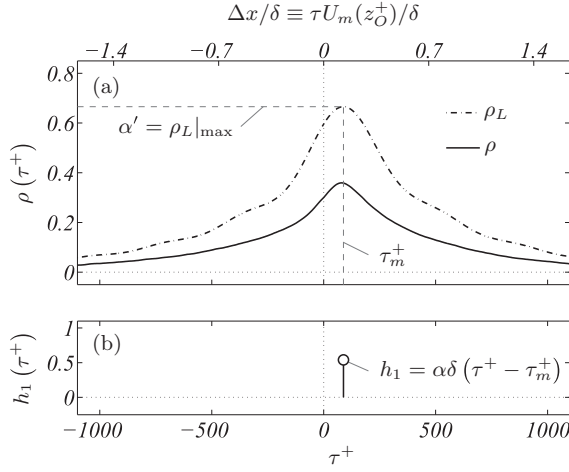


FIG. 7. (a) Temporal two-point correlation for the input and output shown in Fig. 3. Curve ρ_L is the correlation between the large-wavelength pass-filtered signals, u_{OL}^+ and u_L^+ , while ρ is the correlation of the raw signals. (b) Temporal kernel, h_1 , of the single-time LSE in the MMH model.

2. Single-time LSE employed in the MMH model

With SLSE we predict only the energy in the output that is linearly coherent with the input. In retrospect, the MMH model superposition scheme is fundamentally different [20,33]. Before addressing inherent advantages of the SLSE approach, we review the original scheme (Sec. IA) in the context of LSE. Following the nomenclature of our SI/SO example, the superposition constitutes $u_{S,MMH}(t^+) = \alpha u_{OL}^+(t^+ + \tau_m)$. Here subscript L denotes that input u_O^+ is long-wavelength pass-filtered at $\lambda_x^+ > \lambda_{x,F}^+$. A cutoff wavelength is typically taken as $\lambda_{x,F}^+ = 7000$ and is motivated by the fact that this scale seems to separate the inner- and outer-spectral peaks in the boundary layer spectrogram, independent of Reynolds number [12,13]. The superposition term $u_{S,MMH}(t^+)$ indicates that the large-scale component is imposed on the near-wall location through a procedure of scaling (scalar coefficient α) and shifting (a single shift τ_m , expressed as angle $\theta_L = \tan^{-1}[\Delta z / \tau_m / U_m(z_O^+)]$). Both α and τ_m are derived from the correlation of signals $u_{OL}^+(z_O^+)$ and $u_L^+(z^+)$. For the zero-mean fluctuations, the temporal cross-correlation is $R_L(\tau) = \langle u_{OL}(t)u_L(t - \tau) \rangle$ and is normalized in the conventional way, namely, $\rho_L(\tau) = R_L(\tau) / [\sigma(u_{OL})\sigma(u_L)]$, where σ denotes the standard deviation. The normalized correlation of the two large-scale filtered signals, $\rho_L(\tau)$, as well as the two raw signals, $\rho(\tau)$, are shown in Fig. 7(a); a positive shift ($\tau > 0$) implies a temporal lag of the output signal relative to the input. Coefficient α is taken as the maximum of $\rho_L(\tau)$, denoted as α' , scaled by the ratio of standard deviations of the large-scale input and output: $\alpha = \alpha' \sigma(u_L) / \sigma(u_{OL})$ [33,34]. Evidently gain α condenses to the maximum of the two-point correlation, normalized by the large-scale variance of the input, via

$$\alpha = \frac{R_L(\tau)|_{\max}}{\sigma(u_{OL})^2}. \quad (13)$$

Temporal shift τ_m is taken as the temporal shift at which the maximum in the two-point correlation occurs. It is transparent from Eq. (13) that the simple scaling in combination with shift τ_m , for obtaining $u_{S,MMH}$, equates to a single-time LSE scheme [36,37]. Illustratively, we have shown the simplified nature of single-time LSE in Figs. 4–6. Correlation coefficient α' is visualized in Fig. 4 over the range of wavelengths that are considered as large, coherent scales ($\lambda_x^+ > \lambda_{x,F}^+$). More intuitively for the actual estimate, gain α is shown in Fig. 5(a) for the same range of wavelengths; by comparison of Eqs. (7) and (13) it is apparent that $|H_L(f^+)|$ is the frequency-domain, scale-dependent

equivalent of scalar coefficient α . Since only the gain (not the phase shift) is relevant for obtaining the conditional output spectrum, the implication of the scale-independent nature of single-time LSE becomes clear from Fig. 6(b). Similar to the SLSE case discussed in Sec. III B, the output spectrum is scaled with the correlation coefficient, $1/\alpha'$. Intuitively, gain α in the single-time LSE accounts for the correct total energy in the spectral estimate (integral of u spectrum and scaled $u_{S,MMH}$ spectrum are equal for $\lambda_x^+ > \lambda_{xF}^+$), but the spectral energy distribution is, of course, equal to the input spectrum. Concerning the phase, the constant angle θ_L was shown to reasonably approximate the scale-dependent inclination angle [Fig. 5(c)] due to the nondispersive character of the coherent large scales. Summarizing the above, single-time LSE may be captured by a temporal transfer function with a gain α and a shift represented by a delta function at $\tau^+ = \tau_m^+$ [Fig. 7(b)]:

$$h_1(\tau^+) = \alpha \delta(\tau^+ - \tau_m^+). \quad (14)$$

Now, the superposition estimate of the MMH model is obtained by substituting Eq. (14) into Eq. (3):

$$u_{S,MMH}^+(t^+) = \int h_1(\tau^+) u_{OL}^+(t^+ - \tau^+) d\tau^+ = \alpha u_{OL}^+(t^+ + \tau_m^+). \quad (15)$$

Note that here the large-wavelength pass-filtered input velocity signal is employed.

3. Improvements through SLSE

As recognized previously [37,38], the spectral LSE step (Sec. III B) has a number of advantages over single-time LSE (Sec. III B 2). First, the temporal shift between the system's input, $u_o^+(z_o^+)$, and output, $u^+(z^+)$, is not uniquely defined; not all large or coherent scales necessarily obey by one single phase shift. This scale-dependent phase ambiguity is avoided by the spectral technique, since the phase state of the signals is naturally preserved by the spectral estimation coefficients in the linear transfer kernel $\tilde{H}_L(f^+) \in \mathbb{C}$, specifically by its phase [Eq. (8)]. Hence, the burden of having to identify a single shift τ_m^+ , corresponding to the maximum in the temporal cross-correlation, is eliminated.

Second, an empirical scale separation is inherent to the SLSE and is embedded in the scale-dependent gain, $|\tilde{H}_L(f^+)|$. The large-scale input signature that is linearly coherent with the output signal, and thus the location for which the prediction is to be made, is naturally extracted from the raw input signal and superposed with scale-dependent coefficients represented by the spectral gain. This gain function exhibits a gradual roll-off [as observed in Fig. 5(a)] and can be interpreted as an empirically derived scale filter. Thus SLSE eliminates the need for an *a priori* choice of a separation scale, necessary to large-wavelength pass-filter the input and output signals in order to then guide the single-time superposition component of the MMH model.

On the subject of the scale-dependent gain, it was illustrated in the discussion of Fig. 6(b) that the spectrum of the spectral estimate comprises a spectral energy distribution that closely resembles the output spectrum, while the spectrum of the single-time estimate is a scaled-down version of the input spectrum (due to its scalar gain coefficient α). In other words, single-time LSE superposes part of the input energy onto the near-wall position z^+ that is in fact incoherent [where $|\tilde{H}_L| < \alpha$ in Fig. 5(a)] and underestimates part of the energy at the larger wavelengths (where $|\tilde{H}_L| > \alpha$), as is seen from the estimated spectra in Fig. 6(a). It is believed that the improved scale separation in incoherent and coherent scales, as opposed to predefined small and large scales, results in improved predictions at extreme Reynolds numbers that extend orders of magnitude beyond the Reynolds number of the model-calibration experiment (Sec. IV B and onwards).

IV. REFINED MODEL AND CALIBRATION

We can now update the MMH model with the near-wall superposition imprint of coherent scales via the SLSE approach presented in Sec. III B. Model expressions and calibration parameters are provided in Secs. IV A and IV B, respectively, after which we address a few aspects of the new inner-outer interaction model (IOIM) in Sec. IV C.

A. Model expression

Our refined procedure for obtaining the superposition imprint in the near-wall prediction, from an outer-region input, consists of the SLSE as outlined for one prediction location z^+ in Sec. III B; here we simply generalize the concept to all output locations governed by the positions of the inner sensor during the two-point calibration experiment (Table I). Component u_S^+ in Eq. (2) will comprise the SLSE estimate of Eqs. (11) and (12), and transfer kernel $\tilde{H}_L(f^+) \in \mathbb{C}$ now becomes a function of prediction location, z^+ . Hence, the new model expressions are

$$u_p^+(z^+, t^+) = u^*(z^+, t^+) \{1 + \Gamma(z^+) u_S^+(z^+, t^+ - \tau_a^+)\} + u_S^+(z^+, t^+), \quad (16)$$

where component $u_S^+(z^+, t^+)$ is obtained via

$$u_S^+(z^+, t^+) = \mathcal{F}^{-1}\{U_S(z^+; f^+)\} = \mathcal{F}^{-1}\{\tilde{H}_L(z^+; f^+) \mathcal{F}[u_O^+(z_O^+, t^+)]\}. \quad (17)$$

As for the MMH model (Fig. 1), the model's input is a trace of the inner-scaled streamwise velocity fluctuations in the outer region: $u_O^+(z_O^+, t^+)$. An inner-scaled position of $z_O^+ \approx 3.9 \text{Re}_\tau^{1/2}$ resembles the geometric center of the log region [20,60]. Because the model parameters are to be derived (Sec. IV B) relative to this position, any input signal to the model should be acquired in close proximity to z_O^+ at any given Re_τ . Aside from the unfiltered input, the new model requires only kernel $\tilde{H}_L(z^+; f^+)$ to generate the superposition u_S^+ via Eq. (17). Previously, the superposition imprint required scalar parameters $\alpha(z^+)$, $\theta_L(z^+)$ the user-defined separation scale $\lambda_{x_F}^+$.

Once u_S^+ has been found, the original framework of modulation is fused to obtain the new model prediction. For this we require a set, one time series per z^+ , of universal signals, $u^*(z^+, t^+)$, and a location-dependent coefficient, $\Gamma(z^+)$. When comparing the new model expression [Eq. (16)] with the original form [Eq. (2)], it becomes apparent that we introduced a time shift, τ_a^+ , in the superposition component that appears in the modulation term, while the pure superposition term remains unaltered. Amplitude modulation (AM) refers to the temporal variation in small-scale intensity being affected by the larger-scale dynamics (specifically by component u_S^+). A complete review of the modulation and scale interaction in TBLs is beyond the scope of this paper, but notable contributions can be found in the literature (e.g., Refs. [11,13–16]). Specifically, τ_a^+ is the *relative shift* between the superposition imprint and the modulated smaller scales; when $\tau_a^+ = 0$, the superimposed coherent scales at z^+ would be in phase with the large-scale variation of small-scale intensity at that same position. Following the sign convention of Baars *et al.* [17], this shift is negative below the z_O^+ location and implies a *lead* of the modulation signature, relative to the direct imprint of coherent scales. Physically, this shift describes the transition between in-phase modulation in the near-wall region and a preferential alignment of small and large scales in the log region and beyond [17]. Moreover, it is known that the relative shift is governed by inner scaling [61] and is a function of the wall-normal position: $\tau_a^+(z^+)$ is Reynolds number invariant. Implementing $\tau_a^+(z^+)$ in the model enables us to extract a refined universal signal u^* during the calibration step, although implications are virtually unnoticeable since the inner-scaled time shift is relatively small compared to the outer time scale of the coherent scales, particularly at large Re_τ . An empirical function for $\tau_a^+(z^+)$ is taken from Baars *et al.* [17] and comprises a shift that increases in magnitude from $\tau_a^+ \approx -68$ to -210 for $z^+ \approx 10$ to 464. Since u^* and $\Gamma(z^+)$ depend on the new SLSE scheme and the inclusion of τ_a^+ , a new set of model parameters is derived next.

B. Model calibration parameters

Synchronized two-point hot-wire measurements provide the necessary data for model calibration. Quite simply, both the input and output signals are recorded, thus allowing us to extract the empirical model calibration parameters: linear kernel $\tilde{H}_L(z^+; f^+)$, universal signal data $u^*(z^+, t^+)$, and modulation coefficient $\Gamma(z^+)$.

Kernel $\tilde{H}_L(z^+; f^+)$ is found through the concept of Sec. III B with the output signal taken as the time series at each location of the inner sensor: $u^+(z^+, t^+)$. Following Eq. (10), requiring Eqs. (7)

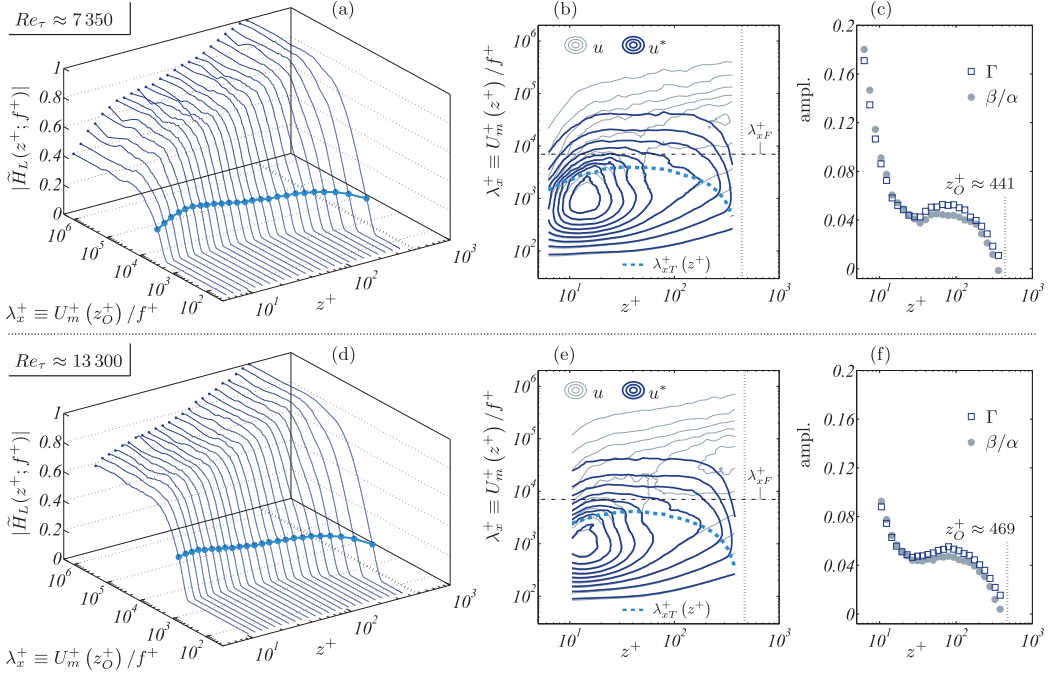


FIG. 8. Model calibration parameters of the new inner-outer interaction model (IOIM). (a) Gain of the linear kernel $\tilde{H}_L(z^+, f^+)$ for every inner-scaled prediction location, z^+ , derived from the $Re_\tau \approx 7350$ calibration data. The line with circle markers corresponds to the coherence-threshold-based scale, λ_{xT}^+ . Inner-scaled wavelength of the spectrogram is computed using the mean velocity at position z_0^+ , $U_m^+(z_0^+)$. (b) Premultiplied energy spectra of the streamwise velocity fluctuations of the universal signal $k_x \phi_{u^* u^*} / U_\tau^2$ (level range 0.2–2.0, level step 0.2); position z_0^+ is shown with the vertical dashed line, and the horizontal dash-dot line represents the common separation scale of $\lambda_{xF}^+ = 7000$. A contour of the spectra of the raw signals, $u(z^+)$, is shown for reference in the background. Inner-scaled wavelength of the spectrogram is computed using the local mean velocity, $U_m^+(z^+)$. (c) Amplitude modulation coefficient $\Gamma(z^+)$, compared to its affiliated parameter group β/α of the MMH model. (d)–(f) Similar to subfigures (a)–(c) but now for the $Re_\tau \approx 13300$ data set.

and (8), the ensemble-averaged, filtered kernel is built for every location of the inner sensor, z^+ . Two complex-valued kernels are constructed from the calibration data at two different Reynolds numbers (Table I); only the kernel’s magnitudes are shown in Figs. 8(a) and 8(d). By direct comparisons of the kernel gains it was validated that they were visually indistinguishable from one another (note the two different gains spans of z^+ in the two data sets). Thus our kernel is effectively independent of the Reynolds number, at least for the two values of Re_τ considered in this study ($Re_\tau \approx 7350$ and $Re_\tau \approx 13300$). Generally, model calibration may be performed at an arbitrary Re_τ , as long as there is an adequate scale separation [12, 13]; both of our calibration data sets have proven to be suitable in that regard.

We will now derive the set of universal signals, $u^*(z^+, t^+)$, and modulation coefficients $\Gamma(z^+)$. Although this part of the model calibration remains unchanged from the procedure described in Mathis *et al.* [33, pp. 545–546], except for the inclusion of $\tau_a^+(z^+)$, we here summarize how this part of the model calibration is carried out. Via a reversed engineering concept, the imprint of the coherent scales is removed from the recorded inner-region signal to obtain a so-called detrended signal:

$$u_d^+(z^+, t^+) = u^+(z^+, t^+) - u_S^+(z^+, t^+). \quad (18)$$

This signal comprises the fluctuations at position z^+ in the absence of any fluctuations that are linearly coherent with z_0^+ . For the calibration data, $u^+(z^+)$ is essentially the predicted signal, and

hence, by combining the model expression [Eqs. (16) and (18)], we obtain the identity:

$$u_d^+(z^+, t^+) = u^*(z^+, t^+) \{1 + \Gamma(z^+) u_S^+(z^+, t^+ - \tau_a^+)\}, \quad (19)$$

where only u^* and Γ are unknowns. The universal signal is envisioned as the inner-scaled velocity fluctuations that would exist in the absence of *any* larger scale dynamics in the outer region. Previous work that led to the predictive model classified this influence of the outer region in the two phenomena of superposition and modulation [8]. While u_d^+ is free of any superposition effect, it has AM signatures embedded within the time series. In order to extract u^* , Eq. (19) is rewritten in explicit form as

$$u^*(z^+, t^+) = \frac{u_d^+(z^+, t^+)}{1 + \Gamma(z^+) u_S^+(z^+, t^+ - \tau_a^+)}, \quad (20)$$

which is iteratively solved for Γ such that u^* does not constitute any AM. Mathis *et al.* [13] introduced an AM coefficient to quantify the degree of AM in a time series in terms of a single scalar metric, dubbed R_a , which is a two-point correlation coefficient between signals $E_L[u^*(z^+, t^+)]$ and $u_S^+(z^+, t^+ - \tau_a^+)$:

$$R_a(u^*) = \frac{\langle E_L[u^*] u_S^+ \rangle}{\sqrt{\langle E_L^2 \rangle} \sqrt{\langle u_S^{+2} \rangle}}. \quad (21)$$

Here $E_L[u^*]$ denotes a large-scale envelope of u^* that is representative of the large-scale variation of the intensity of the fluctuations in u^* . Such an envelope may be obtained via a Hilbert transform [13] or wavelets [17]. Independent of the method, the obtained envelope needs to be long-wavelength pass-filtered to retain only the scales that exist in the modulating signal (signature u_S^+). For this we construct a filter by way of scaling the transfer kernel's gain: its flat region at the larger wavelengths is forced to be ~ 1 . And so we again avoid the user choice of a spectral scale, such as $\lambda_{x_F}^+ = 7000$.

In summary, for every position z^+ , Eq. (20) is now solved for $\Gamma(z^+)$ such that $u^*(z^+, t^+)$ is minimally modulated by $u_S^+(z^+, t^+ - \tau_a^+)$. The corresponding universal signal is then found via Eq. (20) by substituting the obtained value for Γ . Premultiplied spectra of the sets of universal signals are shown in Figs. 8(b) and 8(e), alongside the spectrograms of the acquired signals at z^+ . Similar to \tilde{H}_L , universal signals u^* seem to be Reynolds number invariant over the two values of Re_τ considered for model calibration. Moreover, the spectral properties of u^* have only marginally changed in comparison to Mathis *et al.* [33]. A more elaborate discussion regarding the universal signal characteristics (spectral features and statistical moments) is provided by Mathis *et al.* [33, pp. 547–548]. Finally, profiles of $\Gamma(z^+)$ for both calibration data sets are shown in Figs. 8(c) and 8(f). In agreement to the literature on AM, the curves of $\Gamma(z^+)$ show that AM is strongest near the wall and decreases towards the log region where it is physically interpreted as a relative arrangement of scales (see Ref. [17]). We have also compared the profiles of $\Gamma(z^+)$ to the parameter group β/α , which appeared in the MMH model [Eq. (1)]. The slightly larger value of Γ , relative to β/α , is a result of the inclusion of the modulation-to-superposition shift τ_a^+ , and it is found that Γ was visually identical to β/α when τ_a^+ was excluded (hence, the SLSE upgrade alone was not reflected by a change in Γ). Inclusion of τ_a^+ enabled us to achieve an increased quality of the universal signal: more, potentially all, modulation influence has been removed. Consequently, the modulation coefficient has increased in order to retrieve the original, physically modulated signal from u^* .

C. Remarks about the new predictive model

In comparison to the MMH model, the refined model and its predictions are less driven by user input and comprise an increased accuracy at higher Reynolds numbers. Due to the gradual decay of the empirically derived kernel's gain in spectral space, it is guaranteed that no energy of the input is superimposed on the prediction location that is physically incoherent. Previously this could not be avoided due to an imperfect scale separation into small and large scales (via a user-defined scale

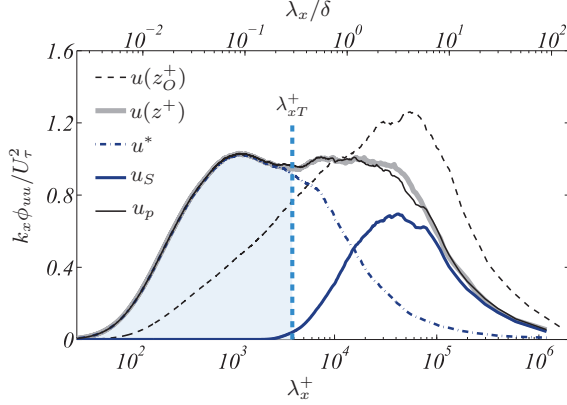


FIG. 9. Illustration of the model prediction for $\text{Re}_\tau \approx 13\,300$: the input is at z_O^+ (Table I) and the output location is $z^+ \approx 58$. Premultiplied spectra are shown of the input [$u(z_O^+)$], the acquired output [$u(z^+)$], the universal signal (u^*), the superposition imprint (u_S), and the prediction (u_p). Inner-scaled wavelength is computed using the local mean velocities, $U_m^+(z^+)$ and $U_m^+(z_O^+)$, following $\lambda_x^+ \equiv U_m^+/f^+$.

λ_{xF}^+). Additionally, it is also guaranteed that all incoherent energy is embedded in the universal signal, which was shown to be Reynolds number invariant. Spectral features of the prediction are illustrated in Fig. 9 for a prediction location of $z^+ \approx 58$ at $\text{Re}_\tau \approx 13\,300$. A comparison between the measured and predicted output spectrum shows an excellent agreement between the two, as should be expected since the prediction is made for the same Re_τ as the calibration data. When decomposing the spectrum of the prediction in its individual components [u^* , interaction $\Gamma u^* u_S$ and u_S , following Eq. (16)] a gradual transition in the composition of the predicted spectrum is evident: the spectrum of u_S prevails at the long wavelengths, whereas u^* contributes at the small scales (and is the sole contributor to the u_p spectrum for $\lambda_x^+ < \lambda_{xT}^+$). When adding the spectra of u^* and u_S , the result is indistinguishable from the u_p spectrum; this implies a negligible contribution from term $\Gamma u^* u_S$, i.e., $\Gamma = O(0.01)$ to $O(0.10)$. However, this term is known to be essential for predicting correct odd-order statistical moments [33].

By including the modulation-to-superposition shift, $\tau_a^+(z^+)$, as well as the SLSE procedure for finding u_S^+ , we achieve universal signals without traces of coherent scales. Henceforth, this eliminates a step that was required in the MMH model (see Ref. [33, p. 549 and Appendix A]): switching the Fourier phase of the model's input signal with the phase of the large-scale signal employed during model calibration. That is, any large-scale input had to be modified to reflect the scale-dependent phase of the calibration data; this ensured that the input is synchronized to the imperfect universal signal that retains some small amount of large-scale information. Mathis *et al.* [33] stated that a higher Reynolds number calibration measurement could avoid the need for this resynchronization of the phase. In hindsight, our current refinements appear to be adequate for not having to consider the phase switch.

We now proceed with a few general remarks about the model. While the superimposed scales constitute the correct phase (preserved in u_S^+), the phase information of the universal small scales is irrelevant; the incoherent nature of small-scale turbulence obstructs the phase preservation in models. Therefore, the predicted signal is spectrally and statistically representative of a physical signal. In terms of the instantaneous validity of the prediction, the superposition component of the signal may be used for real-time applications, such as attempts to actively control large-scale motions in TBLs. Regarding resolution, calibration data were acquired with a hot-wire length of $l^+ \approx 21$ (Table I). Hence, any predictions are made as if they were acquired with a similar inner-scaled hot-wire length. Correction schemes have been developed to add the appropriate amount of energy that is lost due to spatial averaging [62].

Finally, considering a few practicalities [33], the inner-scaled input, $u_o^+(z_o^+)$, may be acquired at an inner-scaled sampling rate ΔT^+ that is different from the calibration data. Therefore, an interpolation or decimation of the input time series to establish the same ΔT^+ is performed prior to any prediction steps in temporal space [additions in Eq. (16)] or spectral space [Eq. (17)]. No specific requirements for the acquisition length of the input exist, other than that the total length of the time series dictates the convergence of the prediction at the longest energetic wavelengths. For predictions at high Re_τ , energies may reside at inner-scaled wavelengths that are larger than the longest wavelength for which the kernel \tilde{H}_L is computed [$\lambda_x^+ \approx 1.5 \times 10^6$, Fig. 8(d)]. In this case, the kernel is extrapolated towards higher wavelengths with a constant amplitude that equals the plateau value of the kernel at large λ_x^+ .

V. MODEL PREDICTIONS

A. Model validation at intermediate Re_τ

Model predictions may be validated with experimental data, as was done extensively for the MMH model using data at five Reynolds numbers ranging from $Re_\tau \approx 2800$ to $Re_\tau \approx 19000$ [33]. These hot-wire anemometry data were obtained with a viscous-scaled wire length of $l^+ \approx 22$, which matches our calibration data (Table I) and thus allows for direct comparisons of the predicted and measured statistics without correcting for hot-wire resolution issues. A complete documentation of these data can be found in Hutchins *et al.* [30].

Since the current work is focused on a refinement of the model, we present only a few validation statistics corresponding to $Re_\tau \approx 2800$ and $Re_\tau \approx 19000$ and employ the $Re_\tau \approx 13300$ calibration data [Figs. 8(d)–8(f)]; predictions using the lower-Reynolds-number calibration data yield similar results, simply due to the universality of the model parameters over the range of Re_τ spanned by the calibration data sets. Two scalar statistics of the streamwise velocity fluctuations are considered first: the turbulence intensity, $\langle u^2 \rangle^+$, and the skewness, S_u . For both Reynolds numbers, we have presented model predictions and direct measurement profiles of these statistics in Figs. 10(a) and 10(c). The measurement location that was used as the model input is marked by the dashed line (residing closest to $z_o^+ = 3.9Re^{1/2}$). All profiles reveal an excellent agreement between the measurements and predictions.

Predictions and measurements of the premultiplied energy spectrograms are presented in Figs. 10(b) and 10(d) for the $Re_\tau \approx 2800$ and $Re_\tau \approx 19000$ conditions, respectively. Generally the predicted spectrogram matches the measured one; similar degrees of similarity were achieved by Mathis *et al.* [33] (more detailed discussions pertaining the validation of model predictions can be found there, including higher-order moments). On the spectrogram plots we have also shown the threshold λ_{xT}^+ that demarcates a shaded region ($\lambda_x^+ < \lambda_{xT}^+$) at which no spectral energy of the input signal is superimposed. Noticeably, the relative contribution to the energy in the spectrogram from this region decreases with increasing Re_τ . Hence, at large Reynolds numbers, the correct prediction of larger scales becomes increasingly important, as is emphasized next in an application of a high-Reynolds-number atmospheric surface layer.

B. Extreme Reynolds number prediction

Having a validated refined model at almost a decade of Reynolds numbers, with calibration parameters that were verified to be invariant with Reynolds number, suggests that the model is a candidate for applications to extreme Reynolds numbers. We here use data of the streamwise velocity fluctuations in an atmospheric surface layer (ASL) at an estimated Kármán number of $Re_\tau \approx 1.4 \times 10^6$ [35]. Time series were recorded at five locations in the range $3470 < z^+ < 42300$. Assuming that the lowest location is in closest proximity to z_o^+ , this time series was taken as the input to the model. A measurement gap starts to reveal itself in model outputs since the prediction locations that we have available were imposed by the inner-scaled sensor positions during the calibration experiment. Model predictions of $\langle u^2 \rangle^+$ and skewness are shown in Figs. 11(a) and 11(b),

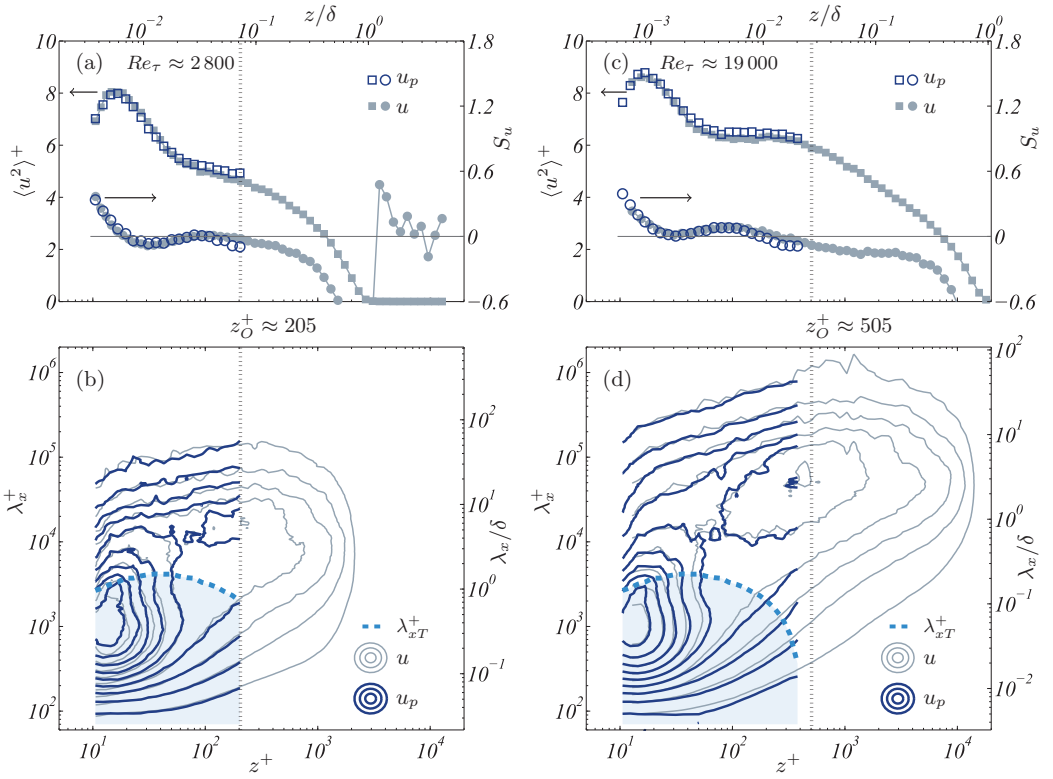


FIG. 10. (a) Prediction of the wall-normal evolution of turbulence intensity, $\langle u^2 \rangle^+$, and skewness, S_u , of the streamwise velocity fluctuations at $Re_\tau \approx 2800$; predictions, open symbols (u_p); measurement profiles, closed symbols (u). The vertical dashed line marks $z_0^+ \approx 3.9Re_\tau^{1/2}$. (b) Premultiplied energy spectra of the streamwise velocity fluctuations $k_x \phi_{uu} / U_\tau^2$ (level range 0.2–2.0, level step 0.2); prediction, u_p contour (thick line); measurement, u contour (thin line). Inner-scaled wavelength of the spectrogram is computed using the local mean velocity, $U_m^+(z^+)$, following $\lambda_x^+ \equiv U_m^+(z^+) / f^+$. (c),(d) Similar to subfigures (a),(b) but now for $Re_\tau \approx 19000$.

respectively. Only a limited amount of measurements are available in the near-wall region of the ASL, and we have plotted various data for comparisons [63–65] and formulations for $\langle u^2 \rangle^+$ proposed by Marusic and Kunkel [66]. Predicted skewness values match the data of Metzger and Klewicki [63] in the inner region. For the inner peak in $\langle u^2 \rangle^+$, residing at $z^+ \approx 15$, an under prediction is observed that may be related to two aspects. First, the hot-wire resolution issue related to a wire length of $l^+ \approx 22$ that propagates from our calibration data into our predictions is known to predominantly affect the inner peak. Second, the input signal has been filtered at the largest scales in an attempt to remove any weather fluctuations that are unavoidable during these field measurements over the salt flats of Utah’s western desert [65]. Any missing energy in the input at large λ_x^+ results in an absence of large-scale energy in the predictions, which would have been predicted by way of the superposition component [Eq. (2)] due to the high gain of the kernel at the large wavelengths. The artificial roll-off at the larger wavelengths is clearly seen from the measured and predicted spectrogram in Fig. 11(c). Aside from that issue, the predicted spectrogram reveals the expected trend in high Reynolds number flows. That is, the coherent large-scales become dominant and generate the outer-spectral peak. Moreover, the measured and predicted spectrograms seem to match accordingly at the lower wavelengths (the dashed lines in the prediction-to-measurement gap, $379 < z^+ < 3470$, are sketched qualitatively).

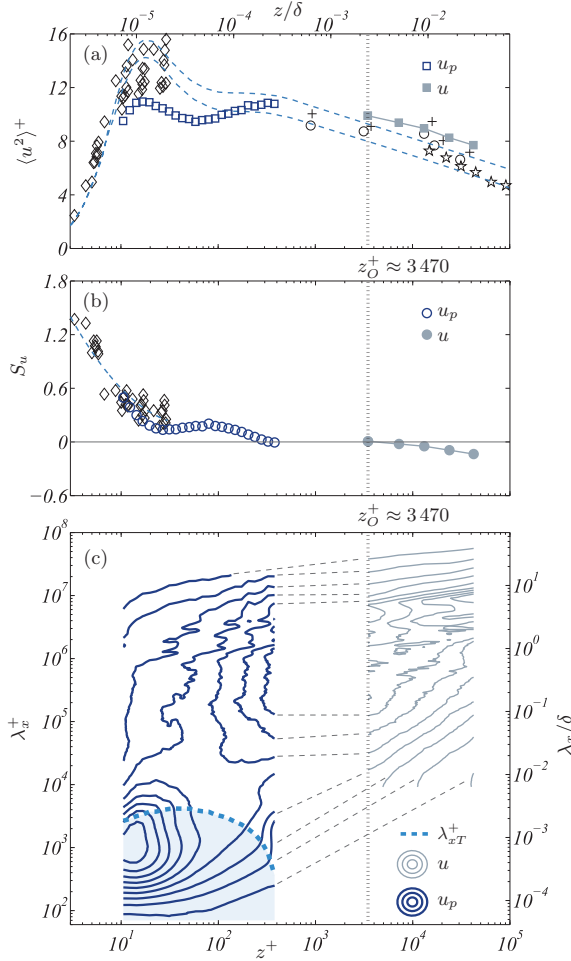


FIG. 11. Prediction of the (a) turbulence intensity, $\langle u^2 \rangle^+$, and (b) skewness, S_u , of the streamwise velocity fluctuations in the ASL at $Re_\tau \approx 1.4 \times 10^6$ [35]; predictions, open symbols (u_p); measurements, closed symbols (u). Data for comparison include (a) *dashed lines*, formulations [66] for $Re_\tau \approx 3.1 \times 10^6$ and 3.7×10^6 ; *diamonds* [63] at $Re_\tau \approx 8.3 \times 10^5$; *circles, plus symbols* [64] $Re_\tau \approx 3.1 \times 10^6$ and 3.8×10^8 ; *star* [65] at $Re_\tau \approx 7.7 \times 10^5$, and (b) *diamonds* [63] at $Re_\tau \approx 8.3 \times 10^5$. The vertical *dashed line* marks the location of the acquired input, z_O^+ . (c) Similar to Fig. 10(b) but now for $Re_\tau \approx 1.4 \times 10^6$. Inner-scaled wavelength of the spectrogram is computed using the local mean velocity, $U_m^+(z^+)$, following $\lambda_x^+ \equiv U_m^+(z^+)/f^+$.

VI. DISCUSSIONS AND CONCLUSIONS

A predictive model for wall-bounded flows, first introduced by Marusic *et al.* [20] and referred here to as the MMH model, has been refined and encompasses four sets of empirically derived model parameters. These parameters are embedded in a model equation, inspired by observations of TBL scale interactions, that allows for predictions of near-wall streamwise velocity fluctuations. A single acquired signal of the velocity fluctuations in the outer region is the only input required. Predicted signals realistically reflect the statistical moments and spectral energy distribution of all scales, and, in addition, the Fourier phase of the coherent scales.

Similar to the MMH model, two additive components form the new model's skeleton: an *amplitude modulation* of universal near-wall velocity fluctuations and a *superposition* of fluctuations that

are known to be coherent between the wall and input positions. We have introduced SLSE to obtain a refined superposition signature u_S^+ ; previously, this was achieved via scaling and shifting the predefined large-scale component of the input time series (single-time LSE). For SLSE, a complex-valued transfer kernel \tilde{H}_L is derived from the once-off model calibration experiment. In conditional predictions, a single SLSE computation then executes three tasks: a filter procedure that retains only the coherent scales of the acquired input (u_O^+), superimposes the input's energy via the scale-dependent gain, and preserves the scale-dependent phase shift. Subsequently, u_S^+ is employed in the second step of the model, comprising modulation of the universal fluctuations u^* ; its modulation strength is ascribed by another model parameter, the modulation coefficient Γ . During modulation, a second refinement of the model accounts for the relative time shift, τ_a^+ , that appears between the coherent superimposed signature at the prediction location and the small-scale modulation envelope, formed by the coherent signal. Finally, summing the superposition signal and modulated universal scales yield the complete prediction u_p^+ .

Model calibration parameters have been validated to be Reynolds number invariant by assessing two-point calibration measurements at $Re_\tau \approx 7350$ and $Re_\tau \approx 13\,300$. Both data sets yielded nominally identical sets of transfer kernels $\tilde{H}_L(z^+; f^+)$, modulation coefficients $\Gamma(z^+)$, universal signals $u^*(z^+, t^+)$, and superposition-to-modulation shifts $\tau_a^+(z^+)$. In model predictions, any scale fluctuations larger than the characteristic inner scales in the universal signal are fused to the model predictions via the superposition components. These larger scales thus span wavelengths from the inner scale to the largest scales that obey outer scaling. Since the universal scales only comprise the truly incoherent scales due to the use of SLSE, all coherent scales are enforced to be sourced from the input. This makes the refined model pervasive for extreme Reynolds number wall turbulence, where the coherent large scales become a predominant factor in their dynamics [8]. Although our paper considers only ZPG TBLs, the model has proven to be promising for filling experimental gaps in geophysical and environmental flows at high Reynolds numbers (as illustrated in the current ASL application in Sec. VB), extreme Reynolds number laboratory experiments on TBLs and other canonical wall-bounded flow configurations [33,67,68], and high Reynolds number LES wall models [34,69].

ACKNOWLEDGMENTS

The authors wish to gratefully acknowledge the Australian Research Council for financial support. We would also like to give special thanks to Dougal T. Squire for experimental support and to Dr. Romain Mathis for helpful discussions about the predictive model. Model calibration parameters with a complementary Matlab script for performing model predictions are available for download at <http://fluids.eng.unimelb.edu.au/#data>.

-
- [1] A. J. Favre, J. J. Gaviglio, and R. Dumas, Structure of velocity space-time correlations in a boundary layer, *Phys. Fluids* **10**, S138 (1967).
 - [2] R. F. Blackwelder and L. S. G. Kovasznay, Time scales and correlations in a turbulent boundary layer, *Phys. Fluids* **15**, 1545 (1972).
 - [3] C. E. Wark and H. M. Nagib, Experimental investigation of coherent structures in turbulent boundary layers, *J. Fluid Mech.* **230**, 183 (1991).
 - [4] B. Ganapathisubramani, E. K. Longmire, and I. Marusic, Characteristics of vortex packets in turbulent boundary layers, *J. Fluid Mech.* **478**, 35 (2003).
 - [5] C. D. Tomkins and R. J. Adrian, Spanwise structure and scale growth in turbulent boundary layers, *J. Fluid Mech.* **490**, 37 (2003).
 - [6] K. C. Kim and R. J. Adrian, Very large-scale motion in the outer layer, *Phys. Fluids* **11**, 417 (1999).

- [7] R. J. Adrian, Hairpin vortex organization in wall turbulence, *Phys. Fluids* **19**, 041301 (2007).
- [8] N. Hutchins and I. Marusic, Evidence of very long meandering structures in the logarithmic region of turbulent boundary layers, *J. Fluid Mech.* **579**, 1 (2007).
- [9] K. N. Rao, R. Narasimha, and M. A. B. Narayanan, The ‘bursting’ phenomenon in a turbulent boundary layer, *J. Fluid Mech.* **48**, 339 (1971).
- [10] G. L. Brown and A. S. W. Thomas, Large structure in a turbulent boundary layer, *Phys. Fluids* **20**, S243 (1977).
- [11] P. R. Bandyopadhyay and A. K. M. F. Hussain, The coupling between scales in shear flows, *Phys. Fluids* **27**, 2221 (1984).
- [12] N. Hutchins and I. Marusic, Large-scale influences in near-wall turbulence, *Philos. Trans. R. Soc. London A* **365**, 647 (2007).
- [13] R. Mathis, N. Hutchins, and I. Marusic, Large-scale amplitude modulation of the small-scale structures in turbulent boundary layers, *J. Fluid Mech.* **628**, 311 (2009).
- [14] D. Chung and B. J. McKeon, Large-eddy simulation of large-scale structures in long channel flow, *J. Fluid Mech.* **661**, 341 (2010).
- [15] M. Guala, M. Metzger, and B. J. McKeon, Interactions within the turbulent boundary layer at high Reynolds number, *J. Fluid Mech.* **666**, 573 (2011).
- [16] B. Ganapathisubramani, N. Hutchins, J. P. Monty, D. Chung, and I. Marusic, Amplitude and frequency modulation in wall turbulence, *J. Fluid Mech.* **712**, 61 (2012).
- [17] W. J. Baars, K. M. Talluru, N. Hutchins, and I. Marusic, Wavelet analysis of wall turbulence to study large-scale modulation of small scales, *Exp. Fluids* **56**, 188 (2015).
- [18] S. I. Chernyshenko, I. Marusic, and R. Mathis, Quasi-steady description of modulation effects in wall turbulence, [arXiv:1203.3714](https://arxiv.org/abs/1203.3714) [physics.flu-dyn].
- [19] C. Zhang and S. I. Chernyshenko, Quasisteady quasihomogeneous description of the scale interactions in near-wall turbulence, *Phys. Rev. Fluids* **1**, 014401 (2016).
- [20] I. Marusic, R. Mathis, and N. Hutchins, Predictive model for wall-bounded turbulent flow, *Science* **329**, 193 (2010).
- [21] A. J. Smits, B. J. McKeon, and I. Marusic, High-Reynolds number wall turbulence, *Annu. Rev. Fluid Mech.* **43**, 353 (2011).
- [22] S. Mochizuki and F. T. M. Nieuwstadt, Reynolds-number-dependence of the maximum in the streamwise velocity fluctuations in wall turbulence, *Exp. Fluids* **21**, 218 (1996).
- [23] I. Marusic, A. K. M. Uddin, and A. E. Perry, Similarity law for the streamwise turbulence intensity in zero-pressure-gradient turbulent boundary layers, *Phys. Fluids* **9**, 3718 (1997).
- [24] D. B. De Graaff, Reynolds-number scaling of the flat-plate turbulent boundary layer, *J. Fluid Mech.* **422**, 319 (2000).
- [25] P. Moin and K. Mahesh, Direct numerical simulation: A tool in turbulence research, *Annu. Rev. Fluid Mech.* **30**, 539 (1998).
- [26] C. Meneveau and J. Katz, Scale-invariance and turbulence models for large-eddy simulation, *Annu. Rev. Fluid Mech.* **32**, 1 (2000).
- [27] U. Piomelli, Large-eddy simulation: Achievements and challenges, *Prog. Aerosp. Sci.* **35**, 335 (1999).
- [28] J. A. Sillero, J. Jiménez, and R. D. Moser, One-point statistics for turbulent wall-bounded flows at Reynolds numbers up to $\delta^+ \approx 2000$, *Phys. Fluids* **25**, 105102 (2013).
- [29] M. Lee and R. D. Moser, Direct numerical simulation of turbulent channel flow up to $\text{Re}_\tau \approx 5200$, *J. Fluid Mech.* **774**, 395 (2015).
- [30] N. Hutchins, T. B. Nickels, I. Marusic, and M. S. Chong, Hot-wire spatial resolution issues in wall-bounded turbulence, *J. Fluid Mech.* **635**, 103 (2009).
- [31] W. K. George and L. Castillo, Zero-pressure-gradient turbulent boundary layer, *Appl. Mech. Rev.* **50**, 689 (1997).
- [32] R. J. Adrian, Closing in on models of wall turbulence, *Science* **329**, 155 (2010).
- [33] R. Mathis, N. Hutchins, and I. Marusic, A predictive inner–outer model for streamwise turbulence statistics in wall-bounded flows, *J. Fluid Mech.* **681**, 537 (2011).

- [34] R. Mathis, I. Marusic, S. I. Chernyshenko, and N. Hutchins, Estimating wall-shear-stress fluctuations given an outer region input, *J. Fluid Mech.* **715**, 163 (2013).
- [35] I. Marusic and W. D. Heuer, Reynolds Number Invariance of the Structure Inclination Angle in Wall Turbulence, *Phys. Rev. Lett.* **99**, 114504 (2007).
- [36] R. J. Adrian, Conditional eddies in isotropic turbulence, *Phys. Fluids* **22**, 2065 (1979).
- [37] D. Ewing and J. H. Citriniti, Examination of a LSE/POD complementary technique using single and multi-time information in the axisymmetric shear layer, in *Proceedings of the IUTAM Symposium on Simulation and Identification of Organized Structures in Flows*, edited by J. N. Sorensen, E. J. Hopfinger, and N. Aubry (IUTAM, Lynby, Denmark, 1999), p. 375.
- [38] C. E. Tinney, F. Coiffet, J. Delville, M. N. Glauser, P. Jordan, and A. M. Hall, On spectral linear stochastic estimation, *Exp. Fluids* **41**, 763 (2006).
- [39] T. B. Nickels, I. Marusic, S. Hafez, and M. S. Chong, Evidence of the k_1^{-1} Law in a High-Reynolds-Number Turbulent Boundary Layer, *Phys. Rev. Lett.* **95**, 074501 (2005).
- [40] W. J. Baars, D. T. Squire, K. M. Talluru, M. R. Abbassi, N. Hutchins, and I. Marusic, Wall-drag measurements of smooth- and rough-wall turbulent boundary layers using a floating element, *Exp. Fluids* **57**, 90 (2016).
- [41] I. Marusic, K. A. Chauhan, V. Kulandaivelu, and N. Hutchins, Evolution of zero-pressure-gradient boundary layers from different tripping conditions, *J. Fluid Mech.* **783**, 379 (2015).
- [42] M. B. Jones, I. Marusic, and A. E. Perry, Evolution and structure of sink-flow turbulent boundary layers, *J. Fluid Mech.* **428**, 1 (2001).
- [43] P. M. Ligrani and P. Bradshaw, Spatial resolution and measurement of turbulence in the viscous sublayer using subminiature hot-wire probes, *Exp. Fluids* **5**, 407 (1987).
- [44] K. M. Talluru, V. Kulandaivelu, N. Hutchins, and I. Marusic, A calibration technique to correct sensor drift issues in hot-wire anemometry, *Meas. Sci. Technol.* **25**, 105304 (2014).
- [45] J. S. Bendat and A. G. Piersol, *Random Data Analysis and Measurement Procedures* (Wiley, New York, 2000).
- [46] M. Schetzen, *The Volterra and Wiener Theories of Nonlinear Systems* (Wiley, New York, 1980).
- [47] A. M. Naguib, C. E. Wark, and O. Juckenhöfel, Stochastic estimation and flow sources associated with surface pressure events in a turbulent boundary layer, *Phys. Fluids* **13**, 2611 (2001).
- [48] N. E. Murray and L. S. Ukeiley, Low-dimensional estimation of cavity flow dynamics, in *42nd Aerospace Sciences Meeting and Exhibit*, AIAA Paper 2004-0681 (AIAA, Reno, NV, 2004).
- [49] N. E. Murray and L. Ukeiley, Modified quadratic stochastic estimation of resonating subsonic cavity flow, *J. Turbulence* **8**, 1 (2007).
- [50] D. Lasagna, L. Fronges, M. Orazi, and G. Iuso, Nonlinear multi-time-delay stochastic estimation: Application to cavity flow and turbulent channel flow, *AIAA J.* **53**, 2920 (2015).
- [51] L. M. Hudy, A. Naguib, and W. M. Humphreys, Stochastic estimation of a separated-flow field using wall-pressure-array measurements, *Phys. Fluids* **19**, 024103 (2007).
- [52] W. J. Baars and C. E. Tinney, Proper orthogonal decomposition-based spectral higher-order stochastic estimation, *Phys. Fluids* **26**, 055112 (2014).
- [53] Y. G. Guezennec, Stochastic estimation of coherent structures in turbulent boundary layers, *Phys. Fluids A* **1**, 1054 (1989).
- [54] R. J. Adrian, P. Moin, and R. D. Moser, Stochastic estimation of conditional eddies in turbulent channel flow, in *Proc. of the Summer Program 1987, Center for Turbulence Research* (Stanford University, 1987), pp. 7–19.
- [55] R. J. Adrian and P. Moin, Stochastic estimation of organized turbulent structure: Homogeneous shear flow, *J. Fluid Mech.* **190**, 531 (1988).
- [56] D. R. Cole and M. N. Glauser, Applications of stochastic estimation in the axisymmetric sudden expansion, *Phys. Fluids* **10**, 2941 (1998).
- [57] J. P. Bonnet, J. Delville, M. N. Glauser, R. A. Antonia, D. K. Bisset, D. R. Cole, H. E. Fiedler, J. H. Garem, D. Hilberg, J. Jeong, N. K. R. Kevlahan, L. S. Ukeiley, and E. Vincendeau, Collaborative testing of eddy structure identification methods in free turbulent shear flows, *Exp. Fluids* **25**, 197 (1998).
- [58] R. K. Otnes and L. Enochson, *Applied Time Series Analysis* (Wiley, New York, 1987).

- [59] K. Chauhan, N. Hutchins, J. Monty, and I. Marusic, Structure inclination angles in the convective atmospheric surface layer, *Boundary-Layer Meteorol.* **147**, 41 (2013).
- [60] I. Marusic, J. P. Monty, M. Hultmark, and A. J. Smits, On the logarithmic region in wall turbulence, *J. Fluid Mech.* **716**, R3 (2013).
- [61] W. J. Baars, N. Hutchins, and I. Marusic, Arrangement of scale-interaction and large-scale modulation in high Reynolds number turbulent boundary layers, *Bull. Am. Phys. Soc.* **60** (2015), BAPS.2015.DFD.L22.7.
- [62] C. C. Chin, N. Hutchins, A. S. H. Ooi, and I. Marusic, Use of direct numerical simulation (DNS) data to investigate spatial resolution issues in measurements of wall-bounded turbulence, *Meas. Sci. Tech.* **20**, 115401 (2009).
- [63] M. M. Metzger and J. C. Klewicki, A comparative study of near-wall turbulence in high and low Reynolds number boundary layers, *Phys. Fluids* **13**, 692 (2001).
- [64] G. J. Kunkel and I. Marusic, Study of the near-wall-turbulent region of the high-Reynolds-number boundary layer using an atmospheric flow, *J. Fluid Mech.* **548**, 375 (2006).
- [65] N. Hutchins, K. Chauhan, I. Marusic, J. Monty, and J. Klewicki, Towards reconciling the large-scale structure of turbulent boundary layers in the atmosphere and laboratory, *Boundary-Layer Meteorol.* **145**, 273 (2012).
- [66] I. Marusic and G. J. Kunkel, Streamwise turbulence intensity formulation for flat-plate boundary layers, *Phys. Fluids* **15**, 2461 (2003).
- [67] R. Mathis, I. Marusic, O. Cabrit, N. L. Jones, and G. N. Ivey, Modeling bed shear-stress fluctuations in a shallow tidal channel, *J. Geophys. Res. (Oceans)* **119**, 3185 (2014).
- [68] R. Mathis, I. Marusic, N. Hutchins, J. Monty, and Z. Harun, Inner-outer interaction predictive model for wall-bounded turbulence subjected to pressure gradient effects, in *Proc. Turbulence and Shear Flow Phenomena 9* (Melbourne, Australia, 2015).
- [69] W. Sidebottom, O. Cabrit, I. Marusic, C. Meneveau, A. Ooi, and D. Jones, Modelling of wall shear-stress fluctuations for large-eddy simulation, in *Proc. 19th Australasian Fluid Mechanics Conf.* (Melbourne, Australia, 2014).